Journal of Alloys and Compounds 720 (2017) 460–465

Contents lists available at ScienceDirect

Journal of Alloys and Compounds

journal homepage: http://www.elsevier.com/locate/jalcom

Study of the $La_{1/2+1/2x}Li_{1/2-1/2x}Ti_{1-x}Al_xO_3$ ($0 \leq x \leq 1$) solid solution. A new example of percolative system in fast ion conductors

María E. Sotomayor [a], Belén Levenfeld [a], Alejandro Varez [a, *], Jesús Sanz [b]

[a] Materials Science and Engineering Department, Carlos III University of Madrid, Avda. Universidad 30, 28911 Leganés, Spain
[b] Materials Science Institute, CSIC, C/ Sor Juana Inés de la Cruz 3, 28049 Cantoblanco, Spain

ARTICLE INFO

Article history:
Received 12 January 2017
Received in revised form
18 May 2017
Accepted 26 May 2017
Available online 28 May 2017

Keywords:
X-ray diffraction
Ionic conduction
Solid-state electrolyte
Li-batteries
Percolative phenomena

ABSTRACT

The synthesis by solid state reaction of new fast ion conductors with perovskite structure was carried out. The crystal structure and electric properties of the $La_{1/2+1/2x}Li_{1/2-1/2x}Ti_{1-x}Al_xO_3$ ($0 \leq x \leq 1$) solid solution were investigated by powder X-ray diffraction and impedance spectroscopy. All compositions of the $La_{1/2}Li_{1/2}TiO_3$-$LaAlO_3$ system, exhibited a single cubic perovskite structure ($a_c \approx 3.87–3.79$ Å; SG *Pm-3m*). The progressive decrease in the unit cell parameters agrees with the lower ionic radii of Al^{3+} in relation to Ti^{4+}, which are allocated in the same octahedra. An upward deviation from the lineal ideal solid solution behavior described by Vegard's law was observed and it was tentatively associated with a volume excess created by solid dilution of non-isovalent cations. Structural features were deduced from Rietveld analysis of XRD patterns. $Ti(Al)O_6$ octahedra are regular and La/vacancies are randomly distributed in A-site of the perovskite. The conductivity decreased almost four orders of magnitude with the Li content. This important decrease on the conductivity was attributed to the charge carrier (Li^+) decrease and the blockade of the perovskite conduction pathways by La ions, according to a three dimensional percolative process. In consequence we present here a new example of percolative system of ionic conductors and the results confirm the important role played by effective vacant A-sites, $n_{eff} = [Li] + n_A$, on Li conductivity of this fast ion conductors family with perovskite structure.

1. Introduction

Interest on high lithium ionic conductors as solid electrolytes in All-Solid-State-Batteries (ASSB) has been intense in the last forty years. Different families of crystalline Li ion conductors have been widely studied [1]. Lanthanum lithium titanate (LLTO) with perovskite structure are among the best Li ion conductors known (10^{-3} S/cm at room temperature) [2] as well as promising candidates for solid electrolytes in ASSB. The peculiar flexibility of the perovskite structure is able to distort in a great variety of ways under chemical substitution in the A and B sites (see Ref. [3] by Stramare et al.). These compositional changes allow modifying the charge carrier number or vacancies involved in the diffusion process. The relationship between conductivity and cation vacancies seemed to be not clear; for instance, focussing on B-site substitution, it was difficult to understand why the replacement of Ti by pentavalent cations such as Nb [4,5], or Ta [6] decreases the ionic conductivity in spite of the increment on A-site vacancy concentration and also the increment on the unit cell parameters. In the same way, the substitutions of Ti by trivalent cations such as Al produce an increase in the conductivity [7], whereas the substitutions by tetravalent cations, Zr, Sn, Mn or Ge, diminish it [8]. All these perovskites have been mainly synthesized by tree methods [3]: solid-state reaction, sol gel synthesis and floating zone. Among them, solid-state reactions are commonly used, which is also one of the most used to prepare inorganic solids [9].

On the other hand, low-temperature neutron diffraction experiments showed that Li ions are located at oxygen square windows of LLTO perovskites [10–12]. Consequently the total amount of vacancies participating in lithium conductivity considerably increases with respect to the nominal A-site vacancies (n_A), being necessary to introduce the concept of effective vacancies $n_{eff} = n_A + [Li]$. The substitution of Li by Na in $Li_{0.5}La_{0.5}TiO_3$ (with $n_A = 0$) reduced drastically the conductivity when the amount of total vacancies decreased below the 3-D percolation threshold ($n_c = 0.31$) of cubic perovskites, indicating that n_{eff} describes better than n_A the amount of vacancies [13,14]. Similar behavior was

* Corresponding author.
E-mail addresses: msotomay@ing.uc3m.es (M.E. Sotomayor), bll@ing.uc3m.es (B. Levenfeld), alvar@ing.uc3m.es (A. Varez), jsanz@icmm.csic.es (J. Sanz).

http://dx.doi.org/10.1016/j.jallcom.2017.05.278
0925-8388/

found in the $La_{1/2-x}Li_{1/2-x}Sr_{2x}TiO_3$ series, where (La^{3+} + Li^{+}) were replaced by Sr^{2+} maintaining as well the charge balance and the amount of nominal n_A vacancies, while the number of effective vacancies is reduced. In this case the percolation threshold was larger (n_c = 0.35) than expected suggesting the existence of an incipient cation segregation at the nanometer scale [15], which has been demonstrated by combining annular bright field (ABF) and high angle annular dark field (HAADF) imaging methods [16].

To go deeper into the study of the percolation process in Li ion conductor perovskites, several compositions of the $La_{1/2}Li_{1/2}TiO_3$-$LaAlO_3$ join of the ternary phase diagram shown in Fig. 1 were synthesized and characterized. Along this series, ($1/2Li^{+}$ + Ti^{4+}) cations were substituted by ($1/2La^{3+}$ + Al^{3+}), preserving both the charge balance and the nominal A-site vacancies (n_A = 0). So, the main goal of this study is to confirm the influence of effective vacancies (n_{eff} = [Li] + n_A), instead of nominal vacancies, on the Li conduction mechanism in these lithium ion conductor perovskites. The full extension of the solid solution has been investigated by means of a combination of X-ray diffraction (XRD) and scanning electron microscopy (SEM) techniques. Structural features of samples, in particular La vacancies distribution, were deduced by Rietveld analysis of XRD patterns, and Li mobility was investigated by impedance spectroscopy. A discussion of the dependence of Li conductivity on the relative Li and vacancies concentrations is here presented.

2. Material and methods

2.1. Sample preparation

Samples of the $La_{1/2+1/2x}Li_{1/2-1/2x}Ti_{1-x}Al_xO_3$ series with x between 0 and 1 (Fig. 1) were prepared by a conventional solid-state reaction, from stoichiometric amounts of high purity Li_2CO_3, La_2O_3, $Al(NO_3)_3 \cdot 9H_2O$ and TiO_2 reagents (purchased from Aldrich). These reagents were ground together in an agate mortar and heated at 800 °C for 12 h (La_2O_3 was previously heated at 700 °C for 4 h for decarbonation). The reground products were isostatic cold-pressed at 200 MPa and heated at 1100 °C for 24 h. Finally, powders were uniaxial pressed and heated again for 6 h at different temperatures depending on their composition (see Table 1). These sintering temperatures were optimized in order to obtain single phases and relative density close to 90% (it can be seen that sintering temperature increases with Al content). The heating rate was decreased to 1 °C/min in order to minimize lithium losses [17,18].

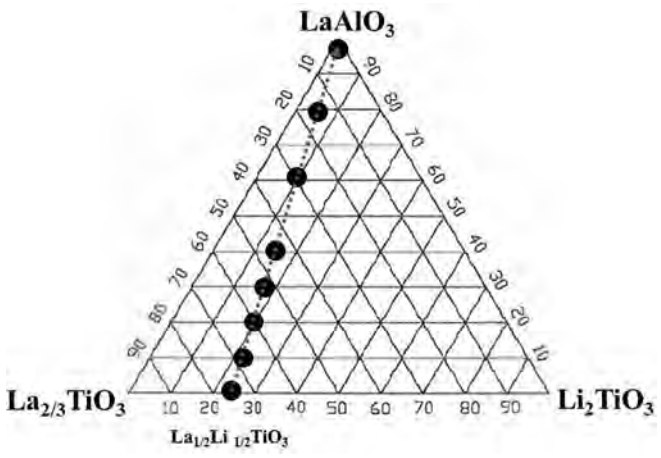

Fig. 1. $La_{2/3}TiO_3$–$LaAlO_3$–Li_2TiO_3 compositional diagram illustrating the Al-doping of LLTO perovskites.

2.2. Samples characterization

XRD powder patterns were recorded on a Philips X'Pert MPD diffractometer equipped with a Cu-K_α radiation source (Fig. 2). This instrument has (θ/2θ) Bragg–Brentano geometry and it is equipped with a curved graphite monochromator. Data were taken with a 0.5° divergence slit, a receiving slit of 0.01° and a set of Soller slits with axial divergence of 1°. Data were recorded between 5 and 120° with a step size of 0.02° and a counting time of 8 s per step. XRD patterns were indexed and analyzed by the Rietveld method using the Fullprof programme [19]. The refinement of XRD patterns involved the lattice and profile parameters determination, background, atomic coordinates, site occupancies and isotropic thermal parameters analysis.

A Philips XL30 scanning electron microscope was employed to observe the microstructure of sintered samples. This microscope is equipped with a backscattered-electron detector (BSE) and an energy-dispersive analyser (EDAX4i). Elemental analyses were performed with a fixed take-off angle, 60 s live time and 15 kV acceleration voltage. Due to the insulator character of materials, samples were covered with a very thin layer of gold by sputtering. For each detected phase, at least five analyses were performed on different crystallites.

Ionic conductivity measurements were performed by Impedance Spectroscopy (IS) using an impedance analyser (Solartron 1260) in the frequency range from 0.1 Hz to 10 MHz. The amplitude of the ac signal applied across the sample was 100 mV. Gold electrodes (Metalor Technologies Ltd.) were painted on polished sintered cylindrical pellets of ~12 mm in diameter and ~1 mm in thickness. Then, prepared pellets were heated to 850 °C for 1 h and then cooled to room temperature. The electrical measurements were performed by using a parallel-plate capacitor configuration. Impedance data were corrected for pellet geometry and capacitance of the conductivity jig.

3. Results and discussion

3.1. X-ray diffraction

XRD patterns of representative samples are shown in Fig. 2. All samples exhibited typical ABO_3 perovskite diffraction patterns. Deduced unit-cell parameters correspond to the primitive cubic cell ($a_p \times a_p \times a_p$) of single-phase perovskites. The existence of single phase for all compositions and the evolution of unit cell parameters (see below) suggest the existence of a solid solution along the series. A very small extra peak associated with $Li_2Ti_3O_7$ was found for x = 0 sample (additional peak labelled with an arrow in the inset of Fig. 2). The amount of these impurities is always estimated to be below 3%. Finally, it is interesting to note that intensity of (100) and (210) reflections at 2θ ~ 23.3° and 53.8° of the single cubic perovskite increases from x = 0 to x = 1. The increase in the intensity of these peaks is a consequence of Al for Ti substitution. Differences on scattering factors of two atoms explain the monotonous increment in intensity of two reflections. For samples with x < 0.2 a very broad and low intense peak, centred at 2θ ~25.5° and labelled with asterisk, was detected. This peak is associated with the doubled perovskite [18,20] indicating that for low Al composition some La-vacancy ordering is still present, but it decreases with the Al content.

The Rietveld analysis of XRD patterns was performed with the Fullprof programme. For the end-member of the series (*i.e.* $La_{0.5}Li_{0.5}TiO_3$) different structural models have been proposed depending on the last cooling rate [18]. We first used a double perovskite with tetragonal symmetry (space group (S.G.) *P4/mmm*) due to the presence of some superstructure peaks (labelled with

Table 1
Nominal composition of $La_{1/2+1/2x}Li_{1/2-1/2x}Ti_{1-x}Al_xO_3$ samples, sintering temperatures and EDS microanalyses results for the single phases. The nominal and experimental La:Al:Ti ratio is also indicated for each composition.

x	Nominal composition	T (°C)	La	Al	Ti	La:Al:Ti nominal	La:Al:Ti experimental
0	$La_{0.5}Li_{0.5}TiO_3$	1300	34.9	–	65.1	0.5:0:1	0.54:0:1
0.1	$La_{0.55}Li_{0.45}Ti_{0.9}Al_{0.1}O_3$	1300	39.6	3.4	56.9	0.61:0.11:1	0.70:0.06:1
0.2	$La_{0.6}Li_{0.4}Ti_{0.8}Al_{0.2}O_3$	1300	41.6	10.7	47.7	0.75:0.25:1	0.83:0.18:1
0.3	$La_{0.65}Li_{0.35}Ti_{0.7}Al_{0.3}O_3$	1350	42.8	10.8	46.5	0.93:0.43:1	0.92:0.23:1
0.4	$La_{0.7}Li_{0.3}Ti_{0.6}Al_{0.4}O_3$	1350	41.8	23.3	34.9	1.17:0.66:1	1.19:0.67:1
0.6[a]	$La_{0.8}Li_{0.2}Ti_{0.4}Al_{0.6}O_3$	1400	44.8	32.5	21.8	2:1.5:1	2.06:1.49:1
0.8	$La_{0.9}Li_{0.1}Ti_{0.2}Al_{0.8}O_3$	1500	47.5	41.8	10.7	4.5:4:1	4.44:3.91:1
1	$LaAlO_3$	1500	50.8	49.2	–	1:1:0	1.03:1:0

[a] For this composition, a secondary phase was detected. The EDS analysis (La:Al:Ti of 8.7:89.7:1.6) indicates that it is compatible with the presence of Al_2O_3.

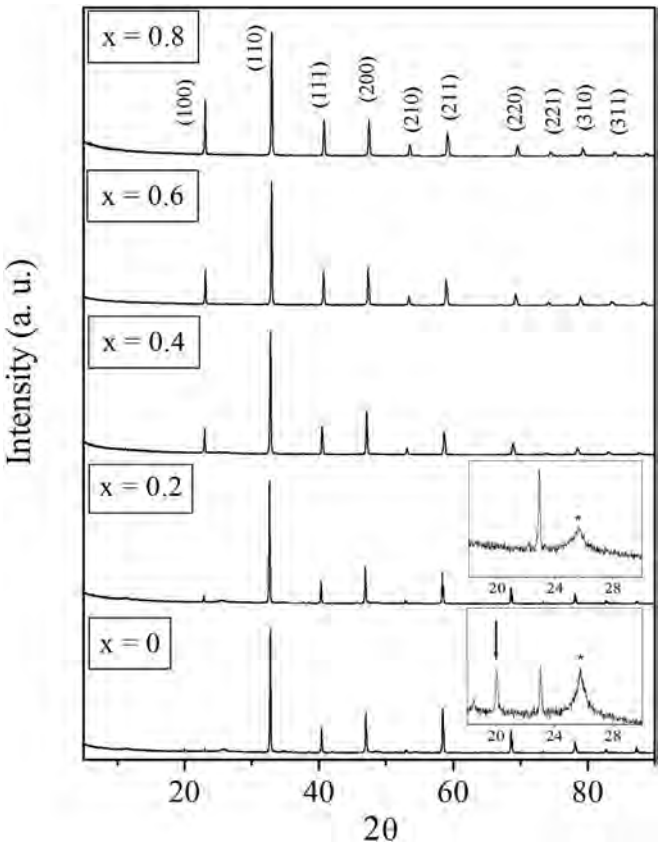

Fig. 2. X-ray diffraction patterns of $La_{1/2+1/2x}Li_{1/2-1/2x}Ti_{1-x}Al_xO_3$ perovskites with compositions x = 0, x = 0.2, x = 0.4, x = 0.6 and x = 0.8. For the sample x = 0, the magnified version of the low 2θ range of the pattern indicates the presence of small amounts of $Li_2Ti_3O_7$ (indicated by the arrow). Also, for samples with x < 0.2 a peak associated with the doubled perovskite is labelled with an asterisk.

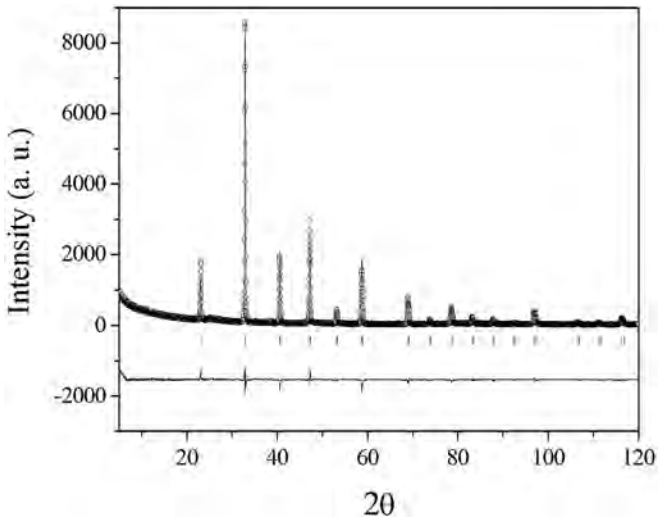

Fig. 3. Rietveld refinement of X-ray pattern of $La_{0.7}Li_{0.3}Ti_{0.6}Al_{0.4}O_3$. The solid line is a fit of calculated to experimental data (open circles). Difference between measured and calculated intensities is given at the bottom. Vertical bars correspond to Bragg positions.

asterisk in inset of Fig. 2) however the absence of sharp superstructure peaks justified the adoption of higher-symmetry. XRD patterns were successfully refined with a single cubic perovskite, S.G. *Pm-3m*, where La are located at *1b* site (1/2,1/2,1/2), Ti at *1a* (0,0,0) and O at *3d* (1/2,0,0). This means that La and vacancies are randomly distributed in A-sites of the perovskite, while Al occupies the octahedral sites, replacing Ti ions. As an example, Fig. 3 shows an accurate fit between measured and calculated intensities for the sample x = 0.4. The rest of the patterns were also successfully refined. A summary of the structural parameters and goodness of fitness for all the samples are given in Table 2. Taking into account the low scattering for the XRD of light element as oxygen and lithium, lower symmetries cannot be discarded, requiring more sensitive diffraction techniques to light elements like neutron diffraction (ND) technique. In fact, the structure of free-Al samples as deduced by neutron diffraction, was rhombohedral (S.G *R-3c*) [10,11], while XRD patterns were successfully refined as a cubic perovskite.

The linear dependence of unit cell parameters with composition often describes solid solutions (Vegard's law). The variation of unit-cell parameter as a function of Al (or Li) content is presented in Fig. 4. In accordance with the ionic radii, lattice parameters of samples decrease with the Al content from 3.8704 Å (x = 0) to 3.7868 Å (x = 1). However, it deviates from the lineal ideal solid solution behavior described by Vegard's law. The upward departure from this law could be associated with a cation disorder of two different cations involved in solid solution ($r^{VI}_{ion}(Ti^{4+}) = 74.5$pm and $r^{VI}_{ion}(Al^{3+}) = 67.5$pm). A similar trend has been reported for the $Li_{1/2-x}Sr_{2x}La_{1/2-x}TiO_3$ solid solution ($0.0625 \leq x \leq 0.25$) and was firstly ascribed to this cation disordering [15] and later on to complex local domains arrangement endotaxially related at nanoscale segregation of two phases in the same crystals [16]. In other systems similar deviation from the Vegard's law were attributed to bond distortions that arise because of the non-isovalent nature of the solid solution $(Ga_{1-x}Zn_x)(N_{1-x}O_x)$ [21] or to the presence of some incipient cation clustering [22].

3.2. Scanning electron microscopy

In order to analyse the homogeneity of samples and to identify

Table 2
Structural parameters deduced from X-ray powder diffraction data of $La_{1/2+1/2x}Li_{1/2-1/2x}Ti_{1-x}Al_xO_3$ perovskites. All the patterns were refined with the cubic *Pm-3m* space group (No 221) and Li atoms were not considered for the refinement.

x	0	0.1	0.2	0.3	0.4	0.6	0.8	1
a (Å)	3.8704(1)	3.8697(1)	3.8617(1)	3.8594(1)	3.8472(1)	3.8290(1)	3.8077(1)	3.7868(1)
B_{La} (Å^2)	0.286(1)	0.599(1)	1.001(1)	0.475(1)	1.286(1)	0.949(1)	1.246(1)	0.721(1)
B_{Al} (Å^2)	–	0.912(2)	1.062(2)	0.515(1)	1.304(1)	0.978(1)	0.988(1)	0.818(1)
B_{Ti} (Å^2)	0.927(1)	0.912(2)	1.062(2)	0.515(1)	1.304(1)	0.978(1)	0.988(1)	–
B_O (Å^2)	1.603(2)	1.412(7)	1.886(4)	1.363(4)	1.407(3)	1.668(3)	1.540(4)	1.291(2)
La (occ)	0.500	0.558	0.642	0.651	0.708	0.825	0.909	1
Al (occ)	–	0.090	0.129	0.297	0.394	0.566	0.797	1
Ti (occ)	1.000	0.909	0.870	0.702	0.607	0.434	0.211	–
O (occ)	3.000	3.000	3.000	3.000	3.000	3.000	3.000	3.000
R_p	10.3	10.5	9.60	8.68	8.03	8.20	8.88	10.4
R_{wp}	13.6	13.4	12.5	11.6	10.7	10.7	11.7	14.3
χ^2	3.01	3.02	2.46	2.27	1.79	2.05	2.18	3.63
R_B	7.80	8.07	10.7	5.43	9.80	6.32	9.93	3.45
R_F	6.70	6.02	4.43	2.95	5.05	2.47	4.52	3.10

B_i denotes the isotropic thermal factors of the different ions; R_p, R_{wp}, χ^2, R_B and R_F are conventional agreement factors given by the refinement programme.

the presence of possible secondary phases, a combination of BSE and EDS detectors was used. Results of the microstructure inspection appear in Fig. 5. Samples with $x \leq 0.2$ exhibited well-developed cubic grains homogeneously distributed throughout the sample. The degree of porosity was insignificant. The average grain size is found to be varying from 2 to 7 μm. For $x = 0.4–0.6$ samples, the edges of the cubic crystal are rounded and the grain size is slightly lower than former compositions, which is indicative that these samples are in a slightly lower sintering stage and the presence of Al increases the sintering temperature. This fact is more significant for samples with higher Al content ($x > 0.6$) where the grain size is clearly lower (≤1 μm) and higher temperatures are required to achieve good compacts. On the other hand, for $x = 0.6$ sample some isolated alumina impurities (less than 0.5%) were observed as black contrast in BSE images. The compositional analysis by EDS (Table 1) of the main phase confirms the nominal stoichiometry of the different samples indicating the good homogeneity of the samples.

3.3. Electrical conductivity

Fig. 6-a shows room-temperature impedance diagrams of $La_{1/2+1/2x}Li_{1/2-1/2x}Ti_{1-x}Al_xO_3$ samples with $x = 0$, 0.1 and 0.3. They consist of one semicircle at high frequency (magnified in Fig. 6-b), one semicircle at intermediate frequencies (main semicircle) and the characteristic low frequency spike. The C′ plot (Fig. 6-c) for the low Al content samples ($x < 0.4$) displayed two well defined plateaux. The high frequency one, with capacitance close to 10^{-11} F/cm, is attributed to the bulk contribution while the intermediate plateau, with capacitance of approximately $10^{-8}–10^{-9}$ F/cm, is related to grain-boundary [23]. In the low frequency area and for one of the samples ($x = 0.1$), a new plateau with capacitance ~10^{-7} F/cm associated to electrode-sample interface response appears. The dependence of the real part of conductivity on the frequency is plotted in Fig. 6-d. The Y′ plot of samples with $x \leq 0.3$ displayed as well a typical behavior of a polycrystalline fast ionic conductor with the two plateaux in the high and the low frequency domain and related to the bulk and ion blocking at the grain boundaries. Thus, the whole analysis of the different formalism confirms that the main semicircle in the impedance plot corresponds to grain-boundary contribution while the high frequency arc is assigned to bulk contribution. In the case of sample with $x = 0.4$, only the main semicircle is seen, being necessary cool down the sample to detect clearly the bulk semicircle. For samples with $x \geq 0.4$, the characteristic dc conductivity *plateau* in the Y′*vs* frequency plots was not detected, suggesting the loss of long-range ionic mobility.

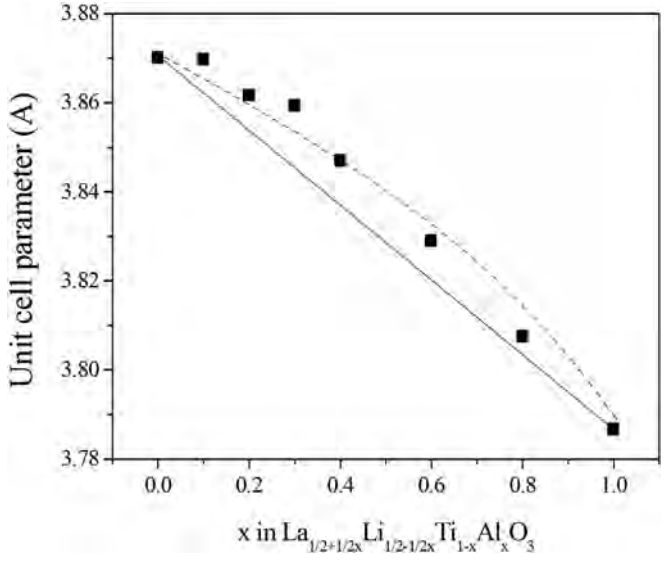

Fig. 4. Compositional dependence of unit cell parameters. Solid line corresponds with Vegard's law.

Dc-conductivity values measured at 300 K are plotted as a function of the amount of effective vacancies (n_{eff}) in Fig. 7. The dc conductivity slightly increases for low substitution degree. Similar results have been found in $La_{1/2-x}Li_{1/2-x}Sr_xTiO_3$, and was attributed to the increase in the unit-cell volume [15,24], which facilitates lithium diffusion. Samples with $x < 0.3$ display values of dc-conductivity in the range of 10^{-3} S/cm, but the conductivity drops several orders of magnitude as the Al content increases. When the Al content increased, dc conductivity at RT is found to be $< 10^{-8}$ S/cm, out of our experimental resolution limit.

In analyzed samples, and considering nominal compositions, all A-sites are occupied by La and Li cations, indicating that there are not nominal vacancies ($n_A = 0$) along the series. Consequently, the observed decrement in conductivity cannot ascribe to the hopping probability of Li to neighbor vacant sites. To understand the observed behavior, we must consider, in agreement with previous works [10–12,25], that Li ions are located in the oxygen square windows between two A-sites. This makes that structural A sites associated with Li ions can be considered as vacant sites, being necessary to consider the concept of effective vacancies, $n_{eff} = [Li] + n_A$, to explain experimental results. Under this

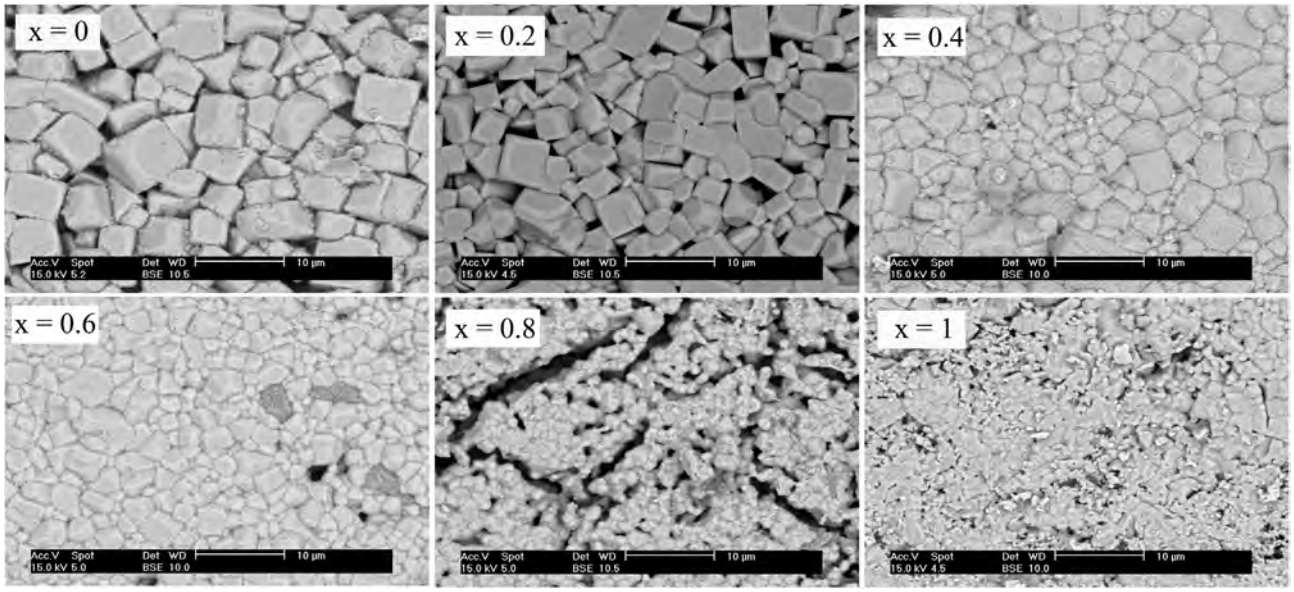

Fig. 5. Scanning electron micrographs of some compositions (x = 0, 0.2, 0.4, 0.6, 0.8 and 1) of the $La_{1/2+1/2x}Li_{1/2-1/2x}Ti_{1-x}Al_xO_3$ perovskites.

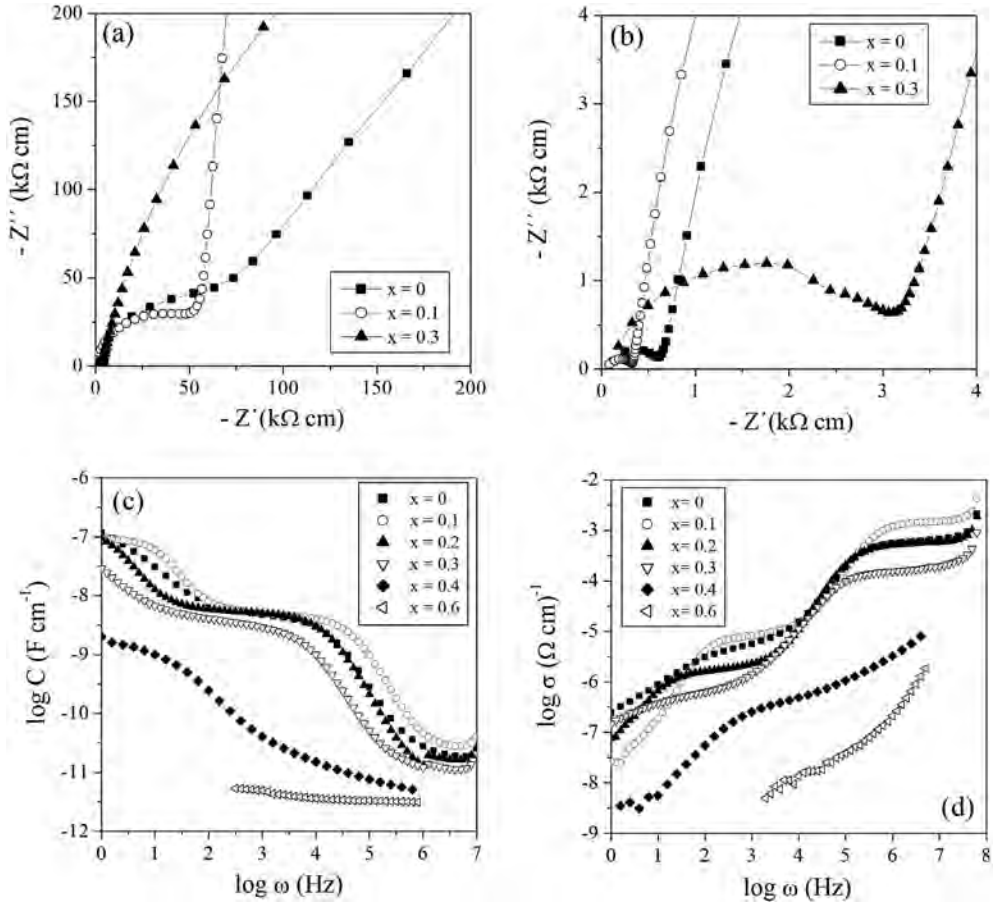

Fig. 6. Samples with different compositions in the $La_{1/2+1/2x}Li_{1/2-1/2x}Ti_{1-x}Al_xO_3$ system: (a, b) Impedance complex plane plots at 300 K; (c) Capacitance data plotted against frequency; (d) Evolution of the conductivity with the frequency.

consideration, observed results can be explained on the basis of a percolative behavior of vacancies. The four orders of magnitude decrement detected in conductivity was related to a decrease on the charge carriers concentration produced by La blocking of conduction pathways of perovskite. The analysis of the conductivity percolation threshold of the series afforded a n_c value of 0.3, in

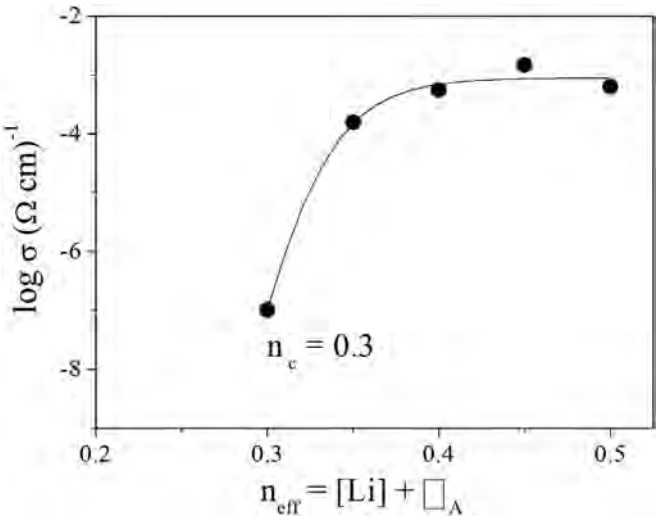

Fig. 7. Conductivity as a function of the amount of effective vacancies (n_{eff}).

agreement with a 3D percolation process of cubic perovskites [26]. Similar observations were described in the other perovskite series such as $Li_{1/2-x}Na_xLa_{1/2}TiO_3$ [13] and $Li_{1/2-x}Sr_{2x}La_{1/2-x}TiO_3$ [15].

4. Conclusions

Different compositions of the $La_{1/2}Li_{1/2}TiO_3$-$LaAlO_3$ system were prepared by solid state reaction (ceramic route). All XRD patterns could be successfully refined with a cubic symmetry, S.G. *Pm-3m*, indicating that the solid solution $La_{1/2+1/2x}Li_{1/2-1/2x}Ti_{1-x}Al_xO_3$ exists along all the compositional range ($0 \leq x \leq 1$) and average structure can be described with a single cubic ($a_p \times a_p \times a_p$) perovskite phase. Considering the limitation of the XRD technique for the analysis of light element, lower symmetries, associated to octahedral tiling, cannot be here discarded. In consequence Li and Ti can be replaced by La and Al in $La_{0.5}Li_{0.5}TiO_3$ according to the mechanism ($1/2Li^+ + Ti^{4+}$) < = > ($1/2La^{3+} + Al^{3+}$). These cation substitutions reduce unit cell parameter from 3.87 to 3.79 Å. Along the solid solution, an upward deviation from Vegard's law was observed, that was ascribed to a cation disordering excess volume. Scanning electron micrographs and EDS analyses showed homogeneous and well-densified samples.

Impedance spectroscopy measurements showed that the conductivity decreased almost four orders of magnitude when the Li content decreased from $x = 0$ to $x = 0.4$. The sharp decrease on the conductivity, for effective vacancies concentration close to 0.3, has been ascribed to the percolative blocking of the three-dimensional conductivity network as a consequence of the additional La incorporation and parallel decrease of vacant A-sites. This result confirms the important role played by effective vacant A-sites, $n_{eff} = [Li] + n_A$, on the Li conductivity of perovskites, which is a consequence of the unusual position of lithium ions at oxygen-square windows of perovskite. A more detailed Li mobility study by NMR and IS (temperature) is now in progress in order to determine the activation energy and diffusion coefficients for the Li mobile ions.

Acknowledgements

Authors thank financial support received from MINECO (MAT2013-46452-C4-3-R and MAT2016-78362-C4-3-R projects), regional CAM government (MATERYENER 3CM, P2013/MIT-2753 program) and the European Commission (Program-IRSES FP7-PEOPLE **Project ID**: 247579 (NANOLICOM)). Also thank Mr. Javier Merino for preparing the samples.

References

[1] A.D. Robertson, A.R. West, A.G. Ritchie, Review of crystalline lithium-ion conductors suitable for high temperature battery applications, Solid State Ion. 104 (1997) 1–11.
[2] Y. Inaguma, L. Chen, M. Itoh, T. Nakamura, T. Uchida, H. Ikuta, M. Wakihara, High ionic-conductivity in lithium lanthanum titanate, Solid State Commun. 86 (1993) 689–693.
[3] S. Stramare, V. Thangadurai, W. Weppner, Lithium lanthanum titanates: A review, Chem. Mater. 15 (21) (2003) 3974–3990.
[4] A.G. Belous, Synthesis and electrophysical properties of novel lithium ion conducting oxides, Solid State Ion. 90 (1996) 193–196.
[5] S. García-Martín, J.M. Rojo, H. Tsukamoto, E. Morán, M.A. Alario-Franco, Lithium-ion conductivity in the novel $La_{1/3-x}Li_{3x}NbO_3$ solid solution with perovskite-related structure, Solid State Ion. 116 (1999) 11–18.
[6] K. Mizumoto, S. Hayashi, Crystal structure and lithium ion conductivity of A-site deficient perovskites $La_{1/3-x}Li_{3x}TaO_3$, J. Ceram. Soc. Jpn. 105 (1997) 713–715.
[7] A. Morata-Orrantia, S. García-Martín, M.A. Alario-Franco, Optimization of lithium conductivity in La/Li titanates, Chem. Mater. 15 (21) (2003) 3991–3995.
[8] H.T. Chung, J.G. Kim, H.G. Kim, Dependence of the lithium ionic conductivity on the B-site ion substitution in $(Li_{0.5}La_{0.5})Ti_{1-x}M_xO_3$ (M = Sn, Zr, Mn, Ge), Solid State Ion. 107 (1998) 153–160.
[9] A.R. West, Solid State Chemistry and its Applications, Wiley, Chichester, U.K, 1984.
[10] J.A. Alonso, J. Sanz, J. Santamaría, C. León, A. Várez, M.T. Fernandez-Díaz, On the location of Li^+ cations in the fast Li-cation conductor $La_{0.5}Li_{0.5}TiO_3$ perovskite, Angew. Chem. Int. Ed. 3 (2000) 619–621.
[11] A. Várez, M.T. Fernandez-Díaz, J.A. Alonso, J. Sanz, Structure of fast ion conductors $Li_{3x}La_{2/3-x}TiO_3$ deduced from powder neutron diffraction experiments, Chem. Mater. 17 (2005) 2404–2412.
[12] M. Yashima, M. Itoh, Y. Inaguma, Y. Morii, Crystal structure and diffusion path in the fast lithium-ion conductor $La_{0.62}Li_{0.16}TiO_3$, J. Amer. Chem. Soc. 127 (2005) 3491–3495.
[13] A. Rivera, C. León, J. Santamaría, A. Várez, O. V'yunov, A.G. Belous, J.A. Alonso, J. Sanz, Percolation-limited ionic diffusion in $Li_{0.5-x}Na_xLa_{0.5}TiO_3$ perovskites ($0 \leq x \leq 0.5$), Chem. Mater. 14 (2002) 5148–5152.
[14] R. Jiménez, A. Rivera, A. Várez, J. Sanz, Li mobility in $Li_{0.5-x}Na_xLa_{0.5}TiO_3$ perovskites ($0 \leq x \leq 0.5$) Influence of structural and compositional parameters, Solid State Ion. 180 (26–27) (2009) 1362–1371.
[15] M.E. Sotomayor, A. Várez, W. Bucheli, R. Jiménez, J. Sanz, Structural characterisation and Li conductivity of $Li_{1/2-x}Sr_{2x}La_{1/2-x}TiO_3$ ($0 < x < 0.5$) perovskites, Ceram. Int. 39 (8) (2013) 9619–9626.
[16] E. García-González, E. Urones-Garrote, A. Várez, J. Sanz, Unravelling the complex nanostructure of $La_{0.5-x}Li_{0.5-x}Sr_{2x}TiO_3$ Li ionic conductors, Dalton Trans. 45 (2016) 7148–7157.
[17] A. Várez, F. García-Alvarado, E. Morán, M.A. Alario-Franco, Microstructural study of $La_{0.5}Li_{0.5}TiO_3$, J. Solid Stat. Chem. 118 (1) (1995) 78–83.
[18] J. Ibarra, A. Várez, C. León, J. Santamaría, L.M. Torres-Martínez, J. Sanz, Influence of composition on the structure and conductivity of the fast ionic conductors $La_{2/3-x}Li_{3x}TiO_3$ ($0.03 \leq x \leq 0.167$), Solid State Ionics 134 (3) (2000) 219–228.
[19] J. Rodríguez-Carvajal, Recent advances in magnetic structure determination by neutron powder diffraction, Phys. B 192 (1993) 55–69. Fullprof Program: Rietveld Pattern Matching Analysis of Powder Patterns, Grenoble, ILL, 1990.
[20] J.L. Fourquet, H. Duroy, M.P. Crosnier-Lopez, Structural and microstructural studies of the series $La_{2/3-x}Li_{3x}\square_{1/3-2x}TiO_3$, J. Solid Stat. Chem. 127 (2) (1996) 283–294.
[21] K. Lee, B.M. Tienes, M.B. Wilker, K.J. Schnitzenbaumer, G. Dukovic, $(Ga_{1-x}Zn_x)(N_{1-x}O_x)$ nanocrystals: visible absorbers with tunable composition and absorption spectra, Nano Lett. 12 (6) (2012) 3268–3272.
[22] M. Castellanos, A.R. West, Deviations from Vegard's law in oxide solid solutions - the systems Li_2TiO_3–MgO and Li_2TiO_3–Na_2TiO_3, J. Chem. Soc. - Faraday Trans. I 76 (1980) 2159–2169.
[23] J.T.S. Irvine, D.C. Sinclair, A.R. West, Electroceramics: characterization by impedance spectroscopy, Adv. Mater. 2 (3) (1990) 132–138.
[24] Y. Inaguma, L. Chen, M. Itoh, T. Nakamura, Candidate compounds with perovskite structure for high lithium ionic conductivity, Solid State Ionics 70–71 (1994) 196–202.
[25] M. Sommariva, M. Catti, Neutron diffraction study of quenched $Li_{0.3}La_{0.567}TiO_3$ lithium ion conducting perovskite, Chem. Mater. 18 (9) (2006) 2411–2417.
[26] D.L. Sidebottom, Dimensionality dependence of the conductivity dispersion in ionic materials, Phys. Rev. Lett. 83 (5) (1999) 983–986.